MDPI

Article

Electronic, Optical, Mechanical and Li-Ion Storage Properties of Novel Benzotrithiophene-Based Graphdiyne Monolayers Explored by First Principles and Machine Learning

Bohayra Mortazavi [1,2,*,†] [ID], Fazel Shojaei [3,†], Masoud Shahrokhi [4], Timon Rabczuk [5], Alexander V. Shapeev [6] and Xiaoying Zhuang [1,5,*]

[1] Department of Mathematics and Physics, Leibniz Universität Hannover, Appelstraße 11, 30167 Hannover, Germany
[2] Cluster of Excellence PhoenixD (Photonics, Optics, and Engineering—Innovation Across Disciplines), Gottfried Wilhelm Leibniz Universität Hannover, 30167 Hannover, Germany
[3] Department of Chemistry, Faculty of Nano and Bioscience and Technology, Persian Gulf University, Bushehr 75169, Iran
[4] Independent Researcher, 69007 Lyon, France
[5] Department of Geotechnical Engineering, College of Civil Engineering, Tongji University, 1239 Siping Road, Shanghai 200070, China
[6] Skolkovo Institute of Science and Technology, Skolkovo Innovation Center, Bolshoy Bulvar, 30, Moscow 143026, Russia
* Correspondence: bohayra.mortazavi@gmail.com (B.M.); zhuang@iop.uni-hannover.de (X.Z.)
† These authors contributed equally to this work.

check for updates

Abstract: Recently, benzotrithiophene graphdiyne (BTT-GDY), a novel two-dimensional (2D) carbon-based material, was grown via a bottom-up synthesis strategy. Using the BTT-GDY lattice and by replacing the S atoms with N, NH and O, we designed three novel GDY lattices, which we named BTHP-, BTP- and BTF-GDY, respectively. Next, we explored structural, electronic, mechanical, optical, photocatalytic and Li-ion storage properties, as well as carrier mobilities, of novel GDY monolayers. Phonon dispersion relations, mechanical and failure behavior were explored using the machine learning interatomic potentials (MLIPs). The obtained HSE06 results reveal that BTX-GDYs (X = P, F, T) are direct gap semiconductors with band gaps in the range of 2.49–2.65 eV, whereas the BTHP-GDY shows a narrow indirect band gap of 0.06 eV. With appropriate band offsets, good carrier mobilities and a strong capability for the absorption of visible and ultraviolet range of light, BTF- and BTT-GDYs were predicted to be promising candidates for overall photocatalytic water splitting. The BTHP-GDY nanosheet, noticeably, was found to yield an ultrahigh Li-ion storage capacity of over 2400 mAh/g. The obtained findings provide a comprehensive vision of the critical physical properties of the novel BTT-based GDY nanosheets and highlight their potential for applications in nanoelectronics and energy storage and conversion systems.

Keywords: graphdiyne; semiconductors; mechanical; optical; machine learning

1. Introduction

Among various 2D carbon-based nanomaterials, the low-symmetry and highly porous hybrid sp and sp^2 graphdiyne families [1] have shown outstanding properties and are being considered as more appealing candidates than graphene for several cutting-edge technologies. Graphdiyne nanosheets show outstanding efficiency for employment in metal-ion batteries [2–4], catalysis [5] and hydrogen storage [6,7] systems. Because of pore-originated soared scattering of phonons in graphdiyne lattices, they normally show almost three orders of magnitude lower lattice thermal conductivity than graphene [8,9], and in combination with high carrier mobility, they can show remarkable efficiency for

thermoelectric energy conversion [10,11]. Graphdiyne nanomembranes, owing to their low-symmetry and -density structural features, are currently among the most highly promising and efficient candidates for next-generation opto-electronics and energy conversion and storage systems. While graphene can be conveniently produced from exfoliation of bulk graphite or via chemical vapor deposition, synthesis of graphdiyne nanomaterials is more complex. Li et al. [12], in 2010, reported the first fabrication of the graphdiyne by devising a cross-coupling reaction. Matsuoka et al. [13], in 2017, made a groundbreaking advance and succeeded in the synthesis of graphdiyne using a novel chemical reaction approach. The aforementioned work facilitated the advancement in this field, and subsequently, Wang et al. [14], Kan et al. [15] and Matsuoka et al. [16] could fabricate novel crystalline boron-, nitrogen- and triphenylene-graphdiyne nanomembranes, respectively. In 2020, Wang et al. [17] and Gao et al. [18] reported the synthesis of large-area pyrenyl- and pyrazinoquinoxaline-graphdiyne, respectively, using a bottom-up chemical synthesis.

In line with the latest trend in the design and synthesis of novel graphdiyne lattices, most recently Pan et al. [19] introduced benzotrithiophene-graphdiyne (BTT-GDY), which was grown via a bottom-up synthesis strategy. According to extensive experimental tests, BTT-GDY nanomembranes were found to be semiconductors with appealing electronic conductivity and charge carrier mobilities as well [19]. Inspired by the exciting lattice of BTT-GDY and by changing the original BTT core molecule, we designed three additional BTT-based graphdiyne systems. We then conducted density functional theory (DFT) calculations to explore the key physical properties of the BTT-based graphdiyne monolayers. For the first time, we employed machine learning interatomic potentials (MLIPs) to investigate the phonon dispersion and complex mechanical responses of graphdiyne networks. Comparisons between DFT- and MLIP-based results for the tensile behavior of the considered graphdiyne lattices reveal the outstanding accuracy of the developed classical models. The presented results confirm the stability and exciting physics of the BTT-based graphdiyne nanosheets and also highlight the robustness of the MLIP-based models in the exploration of complex mechanical/failure responses of highly porous conductive frameworks.

2. Computational Methods

The DFT simulations herein were performed using the Vienna Ab-initio Simulation Package [20,21]. The Perdew–Burke–Ernzerhof (PBE) and generalized gradient approximation (GGA) were employed to treat the effect of exchange–correlation between the electrons along with DFT-D3 [22] van der Waals (vdW) dispersion correction. The plane wave cutoff energy was set to 500 eV with the Monkhorst–Pack [23] k-point method. A vacuum spacing of 15 Å was kept between the two nearest nanosheets to prevent interaction between them in the three-dimensional periodic systems. Atomic positions and simulation box sizes were relaxed until the fulfilment of the energy and force convergence of 10^{-5} eV and 0.01 eV/Å, respectively. For the geometry optimization, we used a $3 \times 3 \times 1$ k-point grid. The first Brillouin zone (BZ) for HSE06 band structure and optical properties calculations was sampled with a $6 \times 6 \times 1$ and $8 \times 8 \times 1$ Γ-centered Monkhorst–Pack [23] mesh, respectively. The deformation potential theory [24] was used to estimate the acoustic phonon scattering limited carrier mobilities within the 2D planes. The electron and hole mobilities were calculated by using $\frac{e\hbar^3 C_{2D}}{K_B T (m^*)^2 (E_i)^2}$, where K_B is the Boltzmann constant, $\hbar$ is the reduced Planck constant, and C_{2D} and m^* are the elastic modulus and the effective mass of the carrier along the transport direction, respectively. E_i is the deformation potential constant, and it is defined as $E_i = \frac{\Delta E_i}{\Delta l / l_0}$, where ΔE_i is the energy shift of i-th edge band in response to the the lattice dialation of $\Delta l / l_0$. The optical absorption was estimated by taking the excitonic effects into consideration with the Tamm–Dancoff approximation (TDHF) via

the Casida equation [25]. The absorption spectrum was subsequently calculated using the following relation:

$$\alpha(\omega) = \sqrt{2}\omega \left[\frac{\sqrt{\varepsilon_1^2 + \varepsilon_2^2} - \varepsilon_1}{2} \right]^{1/2} \qquad (1)$$

Here, ε_2 and ε_1 are the imaginary and real parts of the dielectric function, respectively.

In this work, we passively trained moment tensor potentials (MTPs) [26] to investigate the thermal and mechanical properties at finite temperatures utilizing the MLIP package [27]. The required datasets for the fitting of MTPs were prepared by conducting ab-initio molecular dynamics (AIMD) simulations within the VASP package. AIMD calculations were conducted for strain-free and for four uniaxially loaded unitcells with strains of 10 and 20% for the loading along armchair and zigzag directions, in which the temperature of the systems varied from 300 to 1500 K over 400 time steps. During the AIMD calculations, the systems were heated from 100 to 2000 K over 500 time steps. The complete AIMD trajectories were next subsampled, and around 500 configurations were used to train preliminary MTPs. The accuracies of preliminary fitted MTPs were then examined over the complete dataset, and configurations with worst extrapolation grades [28] were defined and incorporated into the original dataset. The final MTPs with enhanced accuracy and stability were then passively fitted using the improved training dataset. Phonon dispersion relations were also obtained using the fitted MTPs by employing the PHONOPY [29] code using $6 \times 6 \times 1$ supercells. Classical molecular dynamics (CMD) simulations on the basis of MTPs were conducted using the LAMMPS [30] package with the quasi-static loading approach proposed in our recent studies [31,32], with a fixed time step of 0.2 fs to account for the high-frequency vibrations of H atoms.

3. Results and Discussions

First, the structural features of the graphdiyne monolayers explored in this study are discussed. Figure 1 exhibits the primitive cells for four variants of graphdiyne nanosheets, made of structurally similar core molecules of benzotrithiophene (BTT: $C_{12}S_3H_6$), benzotripyrrol (BTP: $C_{12}N_3H_9$), benzotrifuran (BTF: $C_{12}O_3H_6$) and benzotri (1H-Pyrrol-1-yl) (BTHP: $C_{12}N_3H_6$) with C_{3h} symmetry, which are covalently held together by diacetylene linkers. For a consistent reference to these 2D polymers, they are called BTX-GDYs, where X stand for T, P, F and PH. BTX-GDYs are topologically flat lattices, and each hexagonal primitive cell includes two core molecules and three diacetylene linkers. The optimized lattice constants are close to each other, and vary slightly from 22.82 Å for the BTHP-GDY to 23.67 Å for the BTT-GDY monolayer. The predicted lattice constant for the BTT-GDY lattice is considerably close but is still around 2% larger than the experimental data for the multilayer BTT-GDY (a = b = 23.2 Å) [19]. This can be attributed to the fact that under experimental conditions, due to existence of large porosity and thermal effects, the structures do not stay fully flat and contract, resulting in a slightly lower lattice constant. The structural and electronic properties of the BTX-GDYs monolayers are summarized in Table 1, and complete atomic structures are included in the Supplementary Materials. According to the measured bond lengths summarized in Table 1, as expected, covalent interactions are dominant within the planes of the BTX-GDYs nanosheets. For a bird's eye view of chemical interactions within the in-plane and over-the-plane of BTX-GDYs, we calculated the electron localization function (ELF) [33], which is illustrated in Figures 1 and S1, respectively. In Figure 1, the localization pattern (alternating toric and rectangular red cross sections) for alternating between single and triple C-C bonds in diacetylene linkers is also conspicuous. The localization pattern in between those carbon atoms binds BTX and diacetylene linkers, which indicates a charge transfer from the former to the latter. From the Bader charge analysis, we found that BTX molecules in BTPH-, BTP-, BTF- and BTT-GDY transfer on average 0.47, 0.24, 0.38 and 0.44 *e* to each diacetylene linker, respectively. In addition, the iso-surface ELF maps of BTX-GDYs plotted in Figure S1 highlight that polymerization enables efficient delocalization of the π system of the BTX molecules through diacetylene

linkers. This is expected to lead to smaller band gap values for the BTX-GDYs with respect to the HOMO-LUMO gaps of the BTX molecules, and also promote the charge transport within the planes.
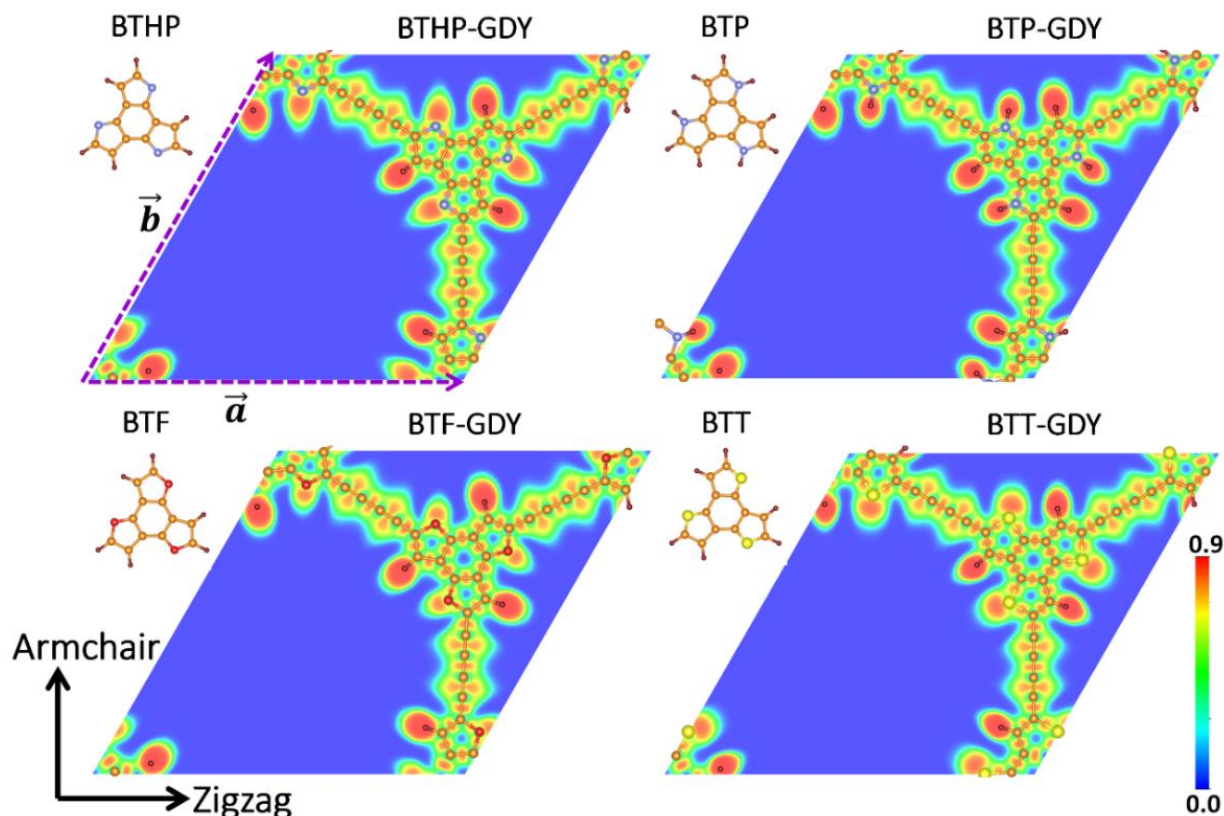
Figure 1. Top views of molecular structures of benzotrithiophene (BTT: $C_{12}S_3H_6$), benzotripyrrol (BTP: $C_{12}N_3H_9$), benzotrifuran (BTF: $C_{12}O_3H_6$) and benzotri(1H-Pyrrol-1-yl) (BTHP: $C_{12}N_3H_6$) and their corresponding graphdiyne (GDY) lattices (BTX-GDY). Horizontal and vertical directions are referred to as zigzag and armchair, respectively. For each one, contour depicts in-plane electron localization function (ELF). Brown, dark brown, blue, red and yellow circles represent C, H, N, O and S atoms, respectively.

**Table 1.** Structural and electronic properties of BTX-GDY, BTX and diacetylene linker.

Polymer	Lattice Constants (Å)	l (Å) [a]	E_g^{PBE} (eV) [b]	E_g^{HSE06} (eV) [c]	E_{VBM}, E_{CBM} (eV) [d]	E_{WF} (eV) [e]	Molecule	E_{H-L} (eV) [f]	E_H, E_L (eV) [g]
BTHP-GDY	22.820	1.24–1.49	0.03	0.06	−6.01, −5.95	5.98	BTHP	1.38	−5.94, −4.56
BTP-GDY	23.101	1.23–1.42	1.83	2.49	−4.87, −2.38	3.63	BTP	4.31	−4.91, −0.60
BTF-GDY	22.885	1.23–1.42	1.94	2.65	−5.63, −2.98	4.31	BTF	4.92	−5.84, −0.92
BTT-GDY	23.670	1.23–1.76	1.88	2.53	−5.62, −3.09	4.36	BTT	4.39	−5.82, −1.44
							Diacetylene	5.87	−7.26, −1.39

[a] The two values correspond to the minimum and maximum bond lengths measured in the primitive cell neglecting the bonds with H atoms. [b] PBE-calculated band gap in the units of eV. [c] HSE06-calculated band gap in eV. [d] Absolute position of VBM and CBM with respect to the vacuum level. [e] Mid-gap work function defined as $E_{WF} = (E_{VBM} + E_{CBM})/2$. [f] HOMO-LUMO gap in eV. [g] Absolute position of HOMO and LUMO states, assuming the vacuum level energy is zero.

After analyzing the structural features of the BTX-GDY nanosheets, we next more elaborately investigated their electronic features. To this goal, electronic band structure calculations were carried out using the standard PBE and more accurate HSE06 functional. For each lattice, the HSE06 electronic band structure, atom-type projected density of states (pDOS), atomic orbital pDOS, contribution of diacetylene linkers to the DOS and

charge density distributions plots for the valence band maximum (VBM) and conduction band minimum (CBM) are illustrated in Figure 2. The corresponding electronic band structures with PBE are included in Figure S2, and band gap values are also summarized in Table 1. According to the presented results, the BTT-GDY monolayer is a direct gap semiconductor at Γ point with an estimated HSE06 (PBE) band gap of 2.53 (1.88) eV. The predicted band gap by HSE06 is 0.15 eV larger than the experimental data (2.38 eV) for the multilayer BTT-GDY [19], which is remarkably close and might be an indication of a limited quantum confinement effect in this system. The band gap of the BTT-GDY monolayer is also appreciably larger than that of the γ-graphdiyne (0.89 eV) [34]. In the BTT-GDY monolayer, both valence and conduction bands (VB, CB) are almost flat and parallel, indicating very large effective masses (62.5 m_0 and 5.26 m_0 for hole and electrons, respectively) and expectably low carrier mobilities. The VBM at the Γ point is, however, two-fold degenerate, and the second VB is highly dispersed along Γ→M and Γ→K, suggesting small effective masses (0.37 m_0) and possibly large hole mobilities. One can clearly observe from Figure 2 that the BTF- and BTP-GDYs show qualitatively similar band structures to the BTT-GDY counterpart, with the minor difference that the CB of the BTP-GDY is more dispersed than that of the other two counterparts. The band gaps of BTF-GDY and BTP-GDY with HSE06 (PBE) were found to be 2.65 (1.94) eV and 2.49 (1.83) eV, respectively, almost insensitive to the chemistry of core molecules. The calculated band gaps are appreciably smaller than the HOMO-LUMO gaps (E_{H-L}) of the BTX and diacetylene molecules, as listed in Table 1. The absolute band edge positions (E_{VBM}, E_{CBM}) are also observed to straddle the HOMO and LUMO energy levels (E_H, E_L) of BTXs and diacetylene molecules (Table 1). For each 2D polymer, the VBM lies energetically close to the HOMO level of the BTX, while the CBM is located appreciably lower than the LUMO level of the BTX (see Table 1). The band structure analysis presented in Figure 2 indicates that for the aforementioned three cases, both the VBM and CBM exhibit a π character made of p_z orbitals of C and hetero-atoms (N, O, S), which are distributed over both the BTX and, at the minimum, over two diacetylene linkers. The VBM can be thought of as a non-bonding interaction between HOMOs of the BTX molecule and the diacetylene linker, while the CBM represents an obvious bonding hybridization between a π state of the BTX molecule and LUMO of diacetylene linkers (shown with dashed red rectangles in charge density distributions plots in Figure S3). This finding explains the underlying mechanism for why almost the same energy levels for the VBM of the BTX-GDY monolayers and HOMO of the BTX molecule and much deeper energy levels for the CBM of BTX-GDY monolayers were observed, as compared to the LUMO of the BTX molecule. To further support the aforementioned discussion, charge density distribution of HOMO and LUMO states of the BTX and diacetylene molecules is shown in Figure S4. In spite of having the same number of electrons per primitive cell and almost similar electronic structures, the BTP-GDY monolayer exhibits a much smaller mid-gap work function (3.64 eV) than those of BTT- and BTF-GDYs, at 4.35 and 4.30 eV, respectively. Unlike these three, BTHP-GDY includes six less electrons. The BTHP-GDY system can be simply generated by removing six hydrogen atoms connected to nitrogen in BTP-GDY's primitive cell. Taking into account that the bands around the Fermi level in BTP-GDY show the π character with no contribution from hydrogen atoms, it may not be surprising that the electronic band structures of the BTP- and BTHP-GDYs look almost similar, except for the mid-gap work function of BTHP-GDY, which is much lower, 5.98 eV. By counting down three bands from the Fermi level of BTP-GDY, the band gap of BTHP-GDY occurs between two closely lying bands with an energy difference of 0.06 (0.03) eV. This gap is indirect with the VBM at K and CBM at the Γ point. The predicted narrow band gap for the BTH-GDY nanosheet may limit its practical applications in electronic devices and photocatalytic chemical processes. The other three BTX-GDY nanosheets, however, are appealing candidates due to their sufficiently large band gaps.
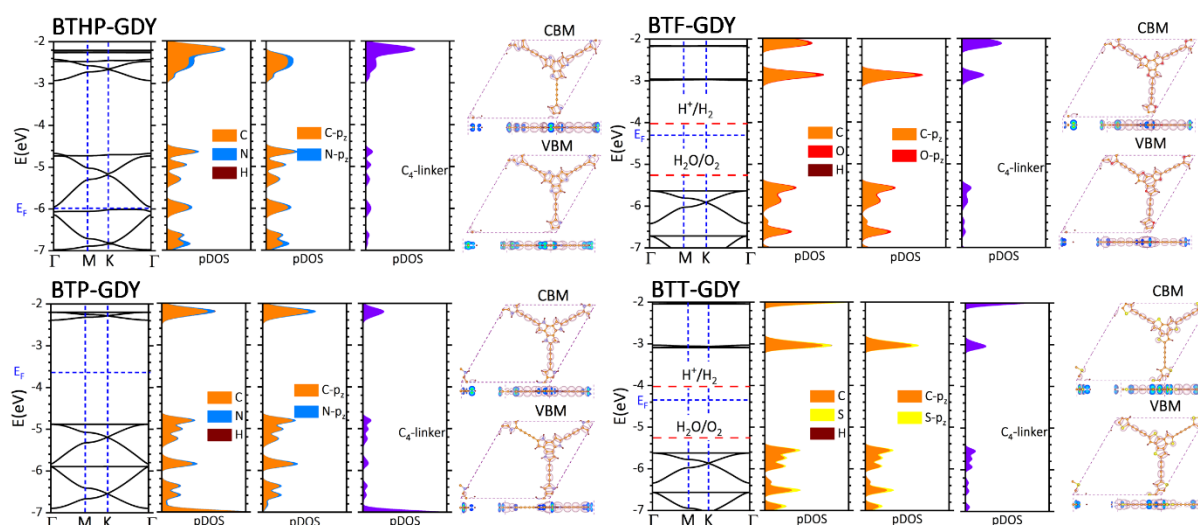
Figure 2. HSE06-based band structures of the BTX-GDY monolayers along with atom-type projected density of states (pDOSs), atomic orbital pDOS, the contribution of diacetylene linkers to the DOS, and charge density distributions of VBM and CBM, respectively. In each case, the bands are aligned with respect to the vacuum level and the Fermi level is set to the middle of band gap. For three BTP-, BTF-, and BTT-GDYs, the oxidation potential of oxygen evolution reaction (OER) and reduction potential of hydrogen evolution reaction (HER) under neutral conditions (pH = 7) are also shown.

After the elaborated investigation of the electronic features of the BTX-GDY monolayers, in the next step, their dynamical stability and mechanical properties will be explored. Before analyzing the phonon dispersion relations, we first examined the accuracy of the developed MLIPs. It is worthwhile to note that the accuracy of MTPs for the evaluation of phonon dispersion relations has been extensively verified in previous studies [29,31]. For this purpose, we conducted biaxial tensile straining employing the developed classical models conducted at 1 K and compared the estimations with the ground-state DFT. Because of the large number of atoms and excessive computational costs of DFT simulations, only primitive hexagonal unit cells were considered for these simulations. With the developed classical models, owing to enhanced computational costs, rectangular supercells were considered in these simulations. In the conducted CMD calculations, the atomic displacements along the out-of-plane direction were fixed in order to keep the consistency of the DFT-based results. In order to plot the results in the standard unit of GPa, a consistent thickness of 3.35 Å is was for the BTX-GDY monolayers based on that for the single-layer graphene. In Figure 3, the stress–strain responses of the BTX-GDY monolayers stretched uniaxially along the armchair and zigzag directions were compared. It is worthwhile to note that since the systems' dimensions along the perpendicular directions of loading are fixed, this results in the formation of two-axial stress condition in these systems. As can be seen for both loading directions, the developed MTPs can reproduce the stress evolution along the zigzag and armchair directions with an exceptional level of accuracy as compared with the computationally expensive DFT counterpart. In Figure S5, we also compare the failure mechanism predicted by the DFT and MLIP method for the BTT-GDY monolayer, which confirms consistent predictions by both approaches. Our analysis of the deformation mechanism reveals that upon the uniaxial straining, the failure in the BTX-GDY nanosheets always initiates along the C-C bonds between the core BTX molecule and diacetylene linkers. It is clear that these 2D systems show considerably close mechanical and failure behaviors.
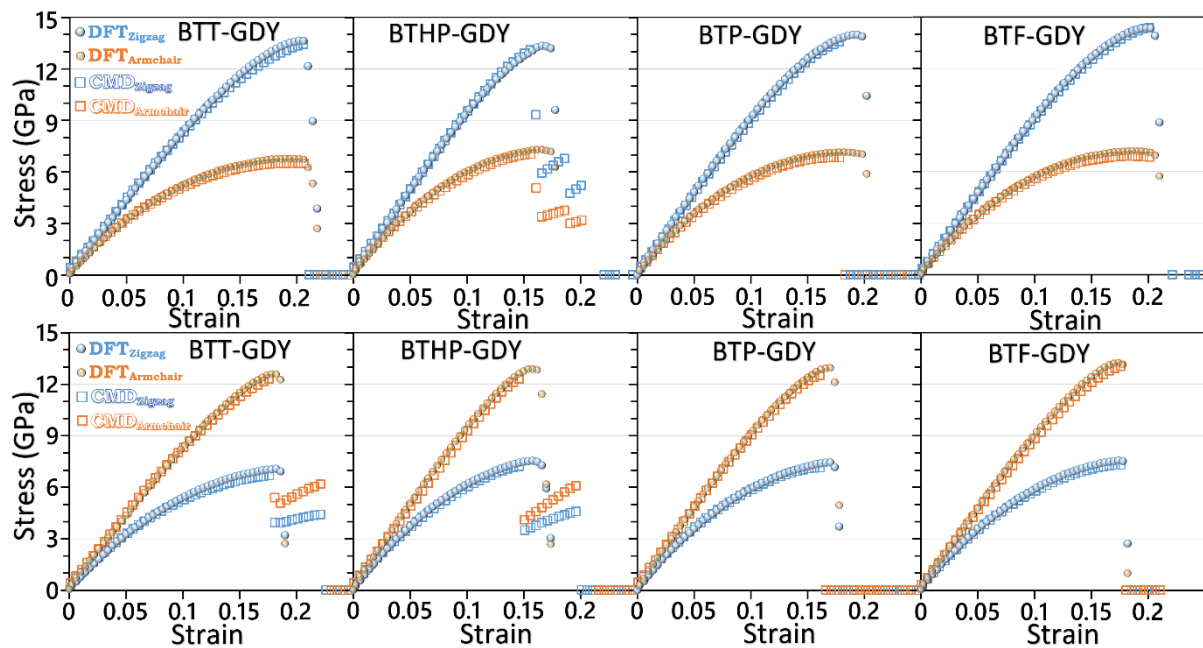
Figure 3. Evolution of stress along the armchair and zigzag direction for the uniaxial straining of the BTX-GDY monolayers elongated along the zigzag (**first row**) and armchair (**second row**) directions by the DFT- and MTP-based CMD models.

We next investigated the dynamical stability of the BTX-GDY monolayers on the basis of phonon dispersion relation calculated using the developed MTPs. In Figure 4, the obtained phonon dispersion relations along the high-symmetry directions of the first Brillouin zone are depicted. Due to the presence of H atoms in these 2D polymers, rather flat optical modes appear at frequencies around 95 THz, which are not illustrated. Like graphene and other 2D lattices, the BTX-GDY monolayers also show three acoustic phonon modes appearing at the Γ point. As it can be seen, none of the acoustic and optical modes in these monolayers exhibit imaginary frequencies, confirming their dynamical stability. It is also noticeable that phonon modes in the considered BTX-GDY monolayers show relatively flat dispersions, which reveal their low group velocities. In addition, remarkable band crossing is conspicuous throughout the entire frequency range for both acoustic and optical modes, revealing high scattering and a short phonon lifetime. The combination of low phonon group velocity and high scattering rates suggest remarkably low lattice thermal conductivity along the BTX-GDY monolayers, which might be appealing for designing next-generation thermoelectric energy conversion systems.
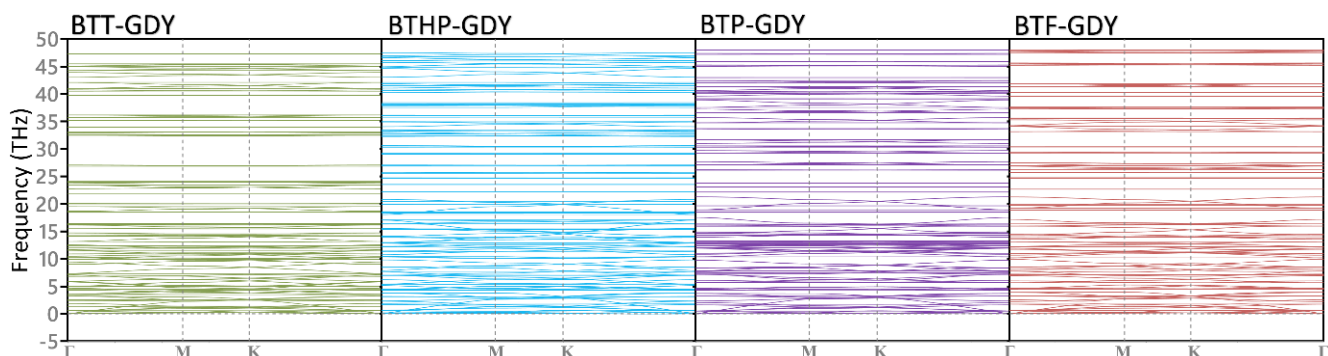

Figure 4. Phonon dispersion relations of the BTX-GDY monolayers. Due to the vibration of the H atoms, flat bands appear at high frequencies (around 95 THz), which are not presented here.

Although the uniaxial straining results highlight remarkable strengths of the BTX-GDY nanosheets, in order to provide a more useful vision concerning the mechanical responses, it is critical to conduct uniaxial tensile simulations. After ensuring the accuracy of the accelerated classical models in the analysis of stress–strain relations, one can utilize them to conduct the uniaxial tensile simulations instead of the expensive DFT counterpart. In Figure 5, the uniaxial stress–strain responses of the BTX-GDY monolayers stretched along the armchair and zigzag directions are compared. On the basis of the developed classical models, the tensile strength of the BTT, BTHP, BTP and BTF-GDY monolayers along the armchair (zigzag) directions was predicted to be 18.1 (14.1), 18.0 (16.2), 18.2 (15.7) and 19.4 (16.2) GPa, respectively. As expected, the predicted values reveal that the mechanical characteristics of the BTX-GDYs show marginal dependency on the chemistry of the core molecules. Nonetheless, for the uniaxial loading along the zigzag direction, the BTT-GDY monolayer clearly shows a lower tensile strength than other lattices. As previously discussed, C-S bonds in the unstrained BTT-GDY monolayer were found to be more than 25% larger than the corresponding C-N and C-O bonds in the other considered lattices, which reveals the softened strength of C-S bonds. As shown in Figure 5b, for the loading along the zigzag direction, the failure in the BTT-GDY monolayer initiates along the C-S bonds, justifying its lower tensile strength. It is also noticeable that the BTX-GDY nanosheets, instead of conventional linear elasticity, yield nonlinear stress–strain relations at low strain levels. The lack of linear elasticity in these systems reveals that the deformation proceeds with a combination of structural deflection and bond stretching. From the structural point of view, because of the existence of rather long diacetylene linkers, these nanosheets include large porosity in their lattice. As such, during the uniaxial tensile loading, sheets more severely contract along the width than densely packed lattices such as graphene, which facilitates the deformation and results in a smooth stress rise at initial stages of the loading. In contrast with conventional materials, at higher strain levels close to the ultimate tensile strength, the stress starts to increase sharply in the BTX-GDY nanosheets. At high strain levels, due to vdW interactions with neighboring atoms, the contraction along the width becomes limited, and thus the bond stretching starts to become the dominant load carrier, resulting in a sharper stress rise by strain. It is also noticeable that along the armchair direction, the BTX-GDY nanosheets clearly exhibit higher tensile strengths and stretchability than along the zigzag direction, which can be also attributed to the structural features. As previously shown, every unit cell in these systems includes three diacetylene linkers, and their configuration with respect to the loading affects the deformation process. As shown in Figure 5b, for the loading along the zigzag direction, for every three diacetylene linkers, one stays exactly perpendicular to the loading during the entire loading process. The aforementioned linker, because of sheet contraction along the width contract, basically does not contribute to the load carrying process. In contrast and as illustrated in Figure 5c, during the loading along the armchair direction, all diacetylene linkers in these systems stretch and contribute to the load transfer, resulting in a higher tensile strength and stretchability as well.

We next explored the possible efficiency of the BTX-GDY monolayers for overall photocatalytic (PC) water splitting reactions. In the PC water splitting process, light is utilized by a semiconductor with specific electro-optical properties to split water into H_2 and O_2 under mild conditions. An appropriate semiconductor for spontaneous PC water splitting, in addition to a large band gap (>1.23 eV), is also supposed to yield band edge positions straddling the water redox potentials ($H^+/H2$ (HER): -4.03 eV vs. vacuum, O_2/H_2O (OER): -5.26 V vs. vacuum, both at pH 7). As shown in Figure 2, only for the BTF- and BTT-GDY monolayers under a neutral condition, the VBM level is less than the oxidation potential of the OER, and the CBM is located higher than the reduction potential of the HER, suggesting they might be promising photocatalysts for overall PC water splitting. A semiconductor with an appropriate band offset for PC water splitting is also expected to show good carrier mobilities able to enhance the efficiency of the energy conversion process. To estimate the electron and hole mobilities within the two promising

candidates of BTF- and BTT-GDY, we employed the conventional deformation potential theory. Table 2 lists the calculated effective masses (m^*), deformation potential constants (C_{2D}) and estimated electron and hole mobilities (μ) for these two polymers. Because of the hexagonal symmetries of the BTF- and BTT-GDY, we only dilated their primitive cells along the zigzag direction in the range of $\pm1.0\%$ and calculated the band edge positions at different degrees of dilation. The predicted acoustic phonon-limited electron mobilities are 6.70 and 4.79 cm^2 V^{-1} s^{-1} for the BTF- and BTT-GDY monolayers, respectively, which are appreciably larger than corresponding values for holes, with almost flat VBs, 0.42 and 0.02 cm^2 V^{-1} s^{-1}, respectively. The estimated carrier mobilities for holes, however, are, as expected, significantly larger than the electron mobilities and are 855 and 451 cm^2 V^{-1} s^{-1} for the BTF- and BTT-GDY monolayers, respectively, indicating that holes are dominant carriers in these nanomaterials. These values are even larger than those predicted for the MoS$_2$ monolayer using the same theory and approximations (~200 cm^2 V^{-1} s^{-1} [35]). It is also worth noting that the experimental calculations for the BTT-GDY also reveal much higher hole mobility than electron mobility (2.34 and 3.35 $\times$ 10^{-2} cm^2 V^{-1} s^{-1} for holes and electrons, respectively [19]). These findings are promising, because a large difference between electron and hole mobilities is appealing for efficient electron–hole separation and higher PC process efficiency.
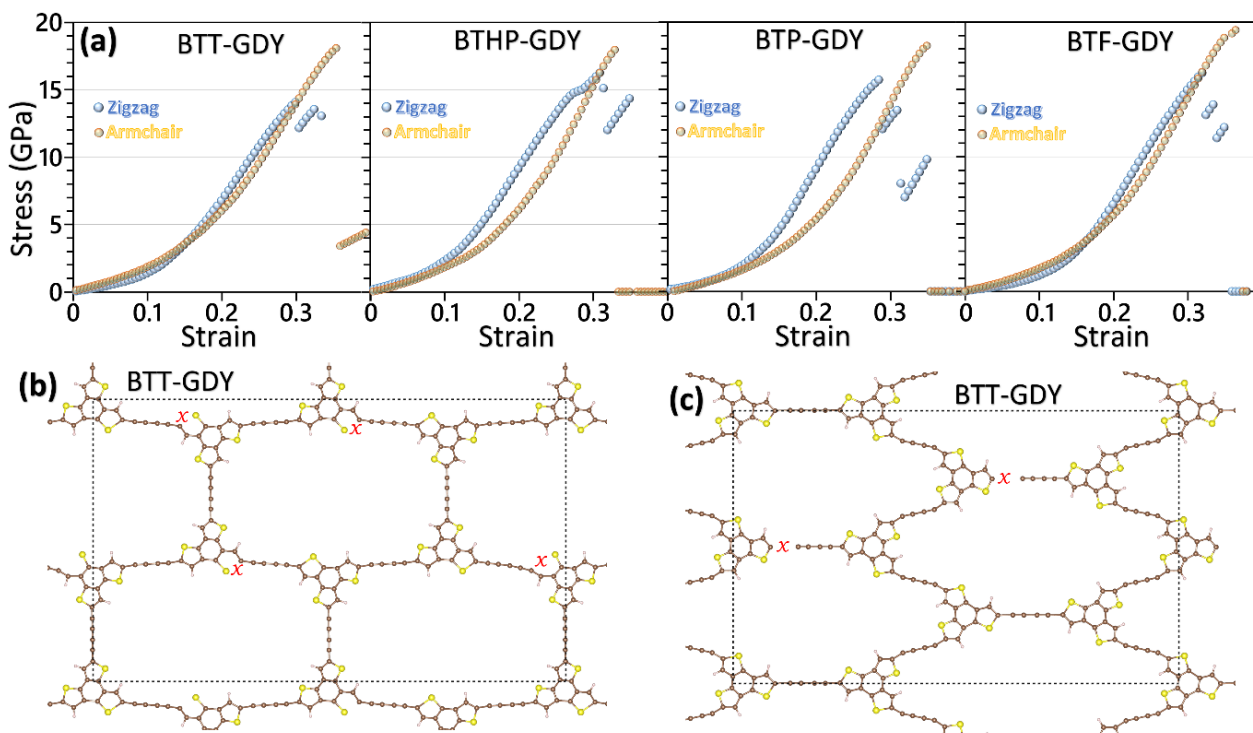

Figure 5. (**a**) Uniaxial stress–strain relations of the BTX-GDY monolayers elongated along the armchair and zigzag directions by the MTP-based CMD model. Failure mechanism of the BTT-GDY for the uniaxial loading along the (**b**) zigzag and (**c**) armchair directions. The "*x*" sign highlights the regions in which initial bond breakages occur.

Table 2. Initial elastic modulus (C_{2D}), effective mass of the electrons and holes (m^*) with respect to the rest mass of an electron (m_0), deformation potential constants of the CBM and VBM ($|E|$) and estimated electron and hole mobilities (μ) for BTF- and BTT-GDYs. Electron and hole mobilities are calculated at 300 K.

	Carrier Type	C_{2D} (N/m)	m^* (m_0)	$|E|$ (eV)	μ (cm^2 V^{-1} s^{-1})
	electron	38	6.50	1.69	6.70
BTF-GDY	heavy hole	38	16.67	2.65	0.42
	light hole	38	0.36	2.72	855.78
	electron	34	5.26	2.34	4.79
BTT-GDY	heavy hole	34	62.5	3.19	0.02
	light hole	34	0.37	3.28	451.44

Other than a large band gap, an appropriate band offset and good carrier mobilities, a semiconductor photocatalyst needs to present a good light absorption within the visible region. We calculated the absorption coefficient (α) for the BTP-, BTT- and BTF-GDY monolayers along the in-plane polarization as a function of wavelength with the HSE06-based RPA method, and the obtained results are plotted in Figure 6. Because of the hexagonal symmetries of BTX-GDY, only the optical properties along the zigzag direction are reported. The absorption coefficients of two different allotropes of the C_3N_4 monolayer, s-triazine-C_3N_4 (gt-C_3N_4) and tri-s-triazine-C_3N_4 (gh-C_3N_4), which are famous for their photocatalytic activity, are also reported. The first peak of α for the BTT-GDY nanosheet occurs at a wavelength of 470 nm while the corresponding first peak for BTP-GDY and BTF-GDY monolayers shifts to the shorter wavelengths (blue shift), occurring at wavelength of 450 nm. These results show the first absorption peak for these novel 2D materials appears in the visible range of light (blue-light wavelength). The first absorption peak for the gh-C_3N_4 and gt-C_3N_4 monolayers occurs at wavelengths of 401 and 372 nm, respectively, which are in the violet-light wavelength. It can also be seen that the absorption coefficients for the BTP-, BTT- and BTF-GDY monolayers in the wavelength range between 375 and 600 nm are larger than those of C_3N_4 monolayers. The high absorption coefficient (~10^5 cm^{-1}) for these novel 2D systems within the visible range of light is highly desirable for visible-light-driven optoelectronic applications.
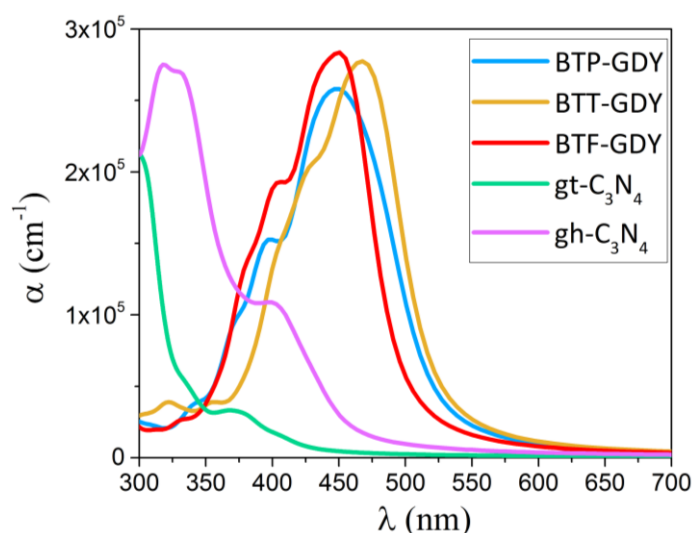

Figure 6. Comparison of optical absorption spectra as a function of wavelength, for the BTP-, BTT- and BTF-GDYs and the well-known C_3N_4 monolayers, s-triazine-C_3N_4 (gt-C_3N_4) and tri-s-triazine-C_3N_4 (gh-C_3N_4), in the UV and visible range (300–700 nm) of light.

Last but not least, graphdiyne nanomembranes are well-known to show outstanding efficiency as anodic materials in metal-ion batteries [2–4,36,37]. In this regard, owing to their light atomic weight and nanoporous structures, graphdiyne nanosheets may show ultrahigh storage capacities for various metal ions. We thus next briefly examine the Li-ion storage capacity of the BTHP-GDY, BTT-GDY and BTF-GDY monolayers. To this end, first, the strongest binding site for a Li adatom adsorption was identified, according to the adsorption energy, E_{ad}:

$$E_{ad} = E_{LiM} - E_M - E_{Li} \tag{2}$$

Here, E_M is the total energy of the pristine monolayers, E_{LiM} is the total energy of the monolayers after the adsorption of a Li atom, and E_{Li} is the per atom energy of the bulk Li. Eight different original adsorption sites were considered, and after the energy optimization with the conjugate gradient method, their corresponding adsorption energies were calculated. The adsorption energy of the Li adatoms over the strongest binding sites for the BTT-GDY and BTF-GDY monolayers was found to be +0.63 and +0.67 eV, respectively. The predicted positive adsorption energies reveal that the Li adatoms prefer to form clusters rather than adsorption over the BTT-GDY and BTF-GDY nanosheets' surfaces. Nitrogen doping is a well-known approach to efficiently boost the anodic performance of carbon-based materials [38–40]. Interestingly, as shown in Figure 7a, the BTHP-GDY nanosheet with active N atoms was found to yield strong adsorption with Li atoms. In order to estimate the storage capacity, the content of Li adatoms over the surface must be increased. To simulate such a process, first all the strongest adsorption sites are gradually filled, which requires six Li atoms over the BTHP-GDY unitcell. As it is clear from Figure 7a, the first and second strongest adsorption sites are very close, and because of the repulsive forces between adatoms, the second position is neglected in this step. On this basis, next, all third strongest adsorption sites over the BTHP-GDY unitcell are filled, which includes 18 Li adatoms. In the final step, using the energy-minimized structure with 18 Li atoms, an additional 12 adatoms are included over the diacetylene linkers on both sides, and 4 Li atoms are placed on both sides of central full-carbon hexagonal rings and consequently the full geometry optimization is carried out. For every Li content, the average adsorption energy is calculated [4], which is illustrated in Figure 7b. As an interesting finding, the average adsorption energy of the BTHP-GDY monolayer with 34 Li adatoms in the unitcell was predicted to be -0.1 eV, which reveals that the metal atoms can still efficiently adsorb over the surface. Bader charge analysis calculations show that upon the adsorption of 34 Li adatoms, they transfer their valence electron to the substrate and become ionized. This finding is consistent with the experimental process, in which the Li ions diffuse from the cathode through the electrolyte and finally adsorb over the anode. It should also be noted that the simulated adsorption process of Li ions is a simplified and rather rough approach. By taking into account that there exists a high probability that other configurations with lower energies but higher adsorbed Li-ion content can form, it is thus clear that herein, estimated storage capacity can only be considered as a lower bound. On this basis, we theoretically predict that the BTHP-GDY nanosheets might be able to yield a Li-ion storage capacity over 2400 mAh/g, which is more than six-fold higher than that of the commercial graphite, at 372 mAh/g [4]. This finding once again reveals the outstanding capacity of the N-based GDY nanosheets for application in rechargeable batteries.
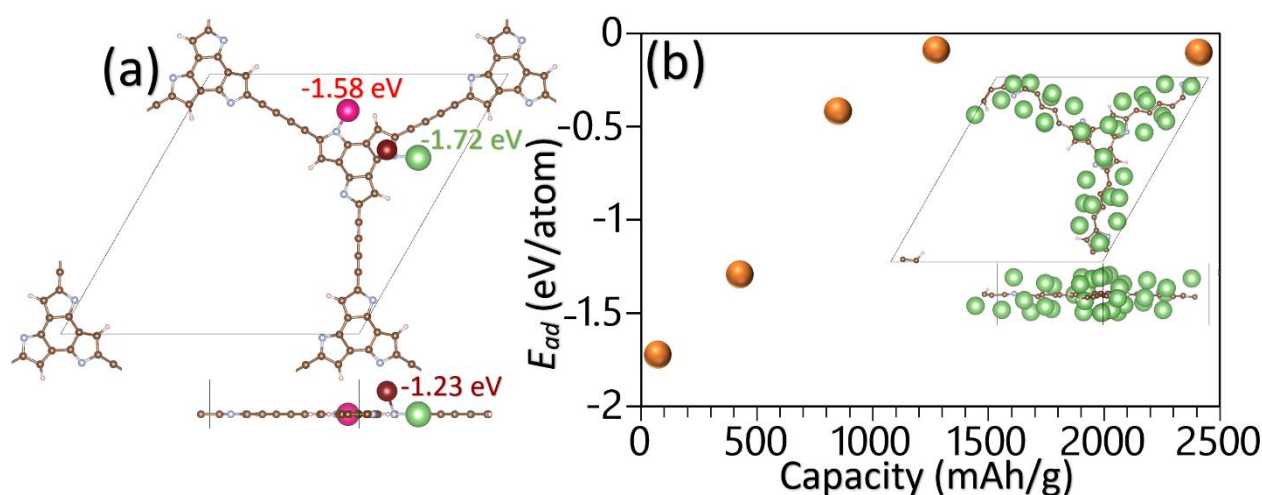
Figure 7. (**a**) Top and side views for the first three strongest binding sites for a Li adatom over the BTHP-GDY monolayer. (**b**) Average absorption energy as a function of Li-ion storage capacity of the BTHP-GDY monolayer. Inset illustrates the top and side views for the energy-minimized BTHP-GDY unitcell with 34 adsorbed Li adatoms.

4. Concluding Remarks

Motivated by the latest advance [19] in the bottom-up synthesis of benzotrithiophene-graphdiyne (BTT-GDY) and by replacing the S atoms in the benzotrithiophene core molecule with N, NH and O atoms, we designed three novel GDY lattices, namely benzotripyrrol (BTP)-, benzotri (1H-Pyrrol-1-yl)) (BTHP)- and benzotrifuran (BTF)-based GDYs. First-principle simulations were next employed to investigate the structural, electronic, mechanical, optical, photocatalytic and Li-ion storage properties of four novel GDY monolayers. In particular, for the first time, machine learning interatomic potentials (MLIPs) were passively fitted to examine dynamical stability and investigate the complex mechanical properties of novel GDY monolayers. The predicted phonon dispersion relations reveal the desirable dynamical stability of the considered GDY nanosheets. Outstanding accuracy of the developed MLIPs in the evaluation of mechanical responses of graphdiyne lattices was confirmed by the comparison with DFT-based stress–strain relations. Elaborated analysis of the mechanical properties confirmed the remarkably high tensile strengths of these novel GDY nanosheets and also revealed that the mechanical characteristics show marginal dependency on the chemistry of the core molecules. The conducted calculations with the HSE06 functional revealed that BTX-GDYs (X = P, F, T) are direct gap semiconductors with band gaps in the range of 2.49–2.65 eV, while BTHP-GDY was predicted to show an indirect and an ultra-narrow band gap of 0.06 eV. The enhanced in-plane conjugation in these 2D polymers was found to enhance large hole mobilities of 855 and 451 cm^2 V^{-1} s^{-1} for the BTF- and BTT-GDY monolayers, respectively. With appropriate electronic band offsets, good carrier mobilities and strong capability for the visible and ultraviolet light absorption, BTF- and BTT-GDYs nanosheets were predicted to be promising photocatalysts for overall water splitting. As an interesting finding, the BTHP-GDY nanosheet was theoretically predicted to yield an ultrahigh Li-ion storage capacity over 2400 mAh/g, more than six-fold higher than that of the commercial graphite. The extensive results reveal outstanding physical properties of the BTT-based GDY nanosheets and also highlight their potential for application in nanoelectronics, photonics, photocatalytic energy conversion and Li-ion energy storage.

Institutional Review Board Statement: Not applicable.

Informed Consent Statement: Not applicable.

Data Availability Statement: The raw data required to reproduce these findings are available upon reasonable request to the corresponding author email.

Conflicts of Interest: The authors have no conflict of interest to declare that are relevant to the content of this article.

References

1. Baughman, R.H.; Eckhardt, H.; Kertesz, M. Structure-property predictions for new planar forms of carbon: Layered phases containing sp^2 and sp atoms. *J. Chem. Phys.* **1987**, *87*, 6687. [CrossRef]
2. Xu, Z.; Lv, X.; Li, J.; Chen, J.; Liu, Q. A promising anode material for sodium-ion battery with high capacity and high diffusion ability: Graphyne and graphdiyne. *RSC Adv.* **2016**, *6*, 25594–25600. [CrossRef]
3. Hussain, T.; Hankel, M.; Searles, D.J. Graphenylene Monolayers Doped with Alkali or Alkaline Earth Metals: Promising Materials for Clean Energy Storage. *J. Phys. Chem. C* **2017**, *121*, 14393–14400. [CrossRef]
4. Bahari, Y.; Mortazavi, B.; Rajabpour, A.; Zhuang, X.; Rabczuk, T. Application of two-dimensional materials as anodes for rechargeable metal-ion batteries: A comprehensive perspective from density functional theory simulations. *Energy Storage Mater.* **2021**, *35*, 203–282. [CrossRef]
5. Lin, Z.Z. Graphdiyne as a promising substrate for stabilizing Pt nanoparticle catalyst. *Carbon* **2015**, *86*, 301–309. [CrossRef]
6. Bartolomei, M.; Carmona-Novillo, E.; Giorgi, G. First principles investigation of hydrogen physical adsorption on graphynes' layers. *Carbon* **2015**, *95*, 1076–1081. [CrossRef]
7. Autreto, P.A.S.; De Sousa, J.M.; Galvao, D.S. Site-dependent hydrogenation on graphdiyne. *Carbon* **2014**, *77*, 829–834. [CrossRef]
8. Hatam-Lee, S.M.; Rajabpour, A.; Volz, S. Thermal conductivity of graphene polymorphs and compounds: From C3N to graphdiyne lattices. *Carbon* **2020**, *161*, 816–826. [CrossRef]
9. Mortazavi, B.; Shahrokhi, M.; Zhuang, X.; Rabczuk, T. Boron-graphdiyne: A superstretchable semiconductor with low thermal conductivity and ultrahigh capacity for Li, Na and Ca ion storage. *J. Mater. Chem. A* **2018**, *6*, 11022–11036. [CrossRef]
10. Sun, L.; Jiang, P.H.; Liu, H.J.; Fan, D.D.; Liang, J.H.; Wei, J.; Cheng, L.; Zhang, J.; Shi, J. Graphdiyne: A two-dimensional thermoelectric material with high figure of merit. *Carbon* **2015**, *90*, 255–259. [CrossRef]
11. Wang, X.M.; Lu, S.S. Thermoelectric transport in graphyne nanotubes. *J. Phys. Chem. C* **2013**, *117*, 19740–19745. [CrossRef]

12. Li, G.; Li, Y.; Liu, H.; Guo, Y.; Li, Y.; Zhu, D. Architecture of graphdiyne nanoscale films. *Chem. Commun.* **2010**, *46*, 3256–3258. [CrossRef] [PubMed]

13. Matsuoka, R.; Sakamoto, R.; Hoshiko, K.; Sasaki, S.; Masunaga, H.; Nagashio, K.; Nishihara, H. Crystalline Graphdiyne Nanosheets Produced at a Gas/Liquid or Liquid/Liquid Interface. *J. Am. Chem. Soc.* **2017**, *139*, 3145–3152. [CrossRef] [PubMed]

14. Wang, N.; Li, X.; Tu, Z.; Zhao, F.; He, J.; Guan, Z.; Huang, C.; Yi, Y.; Li, Y. Synthesis, Electronic Structure of Boron-Graphdiyne with an sp-Hybridized Carbon Skeleton and Its Application in Sodium Storage. *Angew. Chem.* **2018**, *130*, 4032–4037. [CrossRef]

15. Kan, X.; Ban, Y.; Wu, C.; Pan, Q.; Liu, H.; Song, J.; Zuo, Z.; Li, Z.; Zhao, Y. Interfacial Synthesis of Conjugated Two-Dimensional N-Graphdiyne. *ACS Appl. Mater. Interfaces* **2018**, *10*, 53–58. [CrossRef] [PubMed]

16. Matsuoka, R.; Toyoda, R.; Shiotsuki, R.; Fukui, N.; Wada, K.; Maeda, H.; Sakamoto, R.; Sasaki, S.; Masunaga, H.; Nagashio, K.; et al. Expansion of the Graphdiyne Family: A Triphenylene-Cored Analogue. *ACS Appl. Mater. Interfaces* **2018**, *11*, 2730–2733. [CrossRef]

17. Wang, X.-H.; Zhang, Z.-C.; Wang, J.-J.; Chen, X.-D.; Yao, B.-W.; Hou, Y.-X.; Yu, M.-X.; Li, Y.; Lu, T.-B. Synthesis of Wafer-Scale Monolayer Pyrenyl Graphdiyne on Ultrathin Hexagonal Boron Nitride for Multibit Optoelectronic Memory. *ACS Appl. Mater. Interfaces* **2020**, *12*, 33069–33075. [CrossRef]

18. Gao, L.; Ge, X.; Zuo, Z.; Wang, F.; Liu, X.; Lv, M.; Shi, S.; Xu, L.; Liu, T.; Zhou, Q.; et al. High Quality Pyrazinoquinoxaline-based Graphdiyne for Efficient Gradient Storage of Lithium Ions. *Nano Lett.* **2020**, *20*, 7333–7341. [CrossRef]

19. Pan, Q.; Chen, X.; Li, H.; Chen, S.; Zheng, X.; Liu, H.; Li, B.; Zhao, Y. Preparation of crystalline benzotrithiophene-based two-dimensional graphdiyne analogue. *2D Mater.* **2021**, *9*, 14001. [CrossRef]

20. Kresse, G.; Furthmüller, J. Efficient iterative schemes for ab initio total-energy calculations using a plane-wave basis set. *Phys. Rev. B* **1996**, *54*, 11169–11186. [CrossRef]

21. Perdew, J.P.; Burke, K.; Ernzerhof, M. Generalized Gradient Approximation Made Simple. *Phys. Rev. Lett.* **1996**, *77*, 3865–3868. [CrossRef] [PubMed]

22. Grimme, S.; Antony, J.; Ehrlich, S.; Krieg, H. A consistent and accurate ab initio parametrization of density functional dispersion correction (DFT-D) for the 94 elements H-Pu. *J. Chem. Phys.* **2010**, *132*, 154104. [CrossRef] [PubMed]

23. Monkhorst, H.; Pack, J. Special points for Brillouin zone integrations. *Phys. Rev. B* **1976**, *13*, 5188–5192. [CrossRef]

24. Bardeen, J.; Shockley, W. Deformation potentials and mobilities in non-polar crystals. *Phys. Rev.* **1950**, *80*, 72. [CrossRef]

25. Sander, T.; Maggio, E.; Kresse, G. Beyond the Tamm-Dancoff approximation for extended systems using exact diagonalization. *Phys. Rev. B* **2015**, *92*, 45209. [CrossRef]

26. Shapeev, A.V. Moment tensor potentials: A class of systematically improvable interatomic potentials. *Multiscale Model. Simul.* **2016**, *14*, 1153–1173. [CrossRef]

27. Novikov, I.S.; Gubaev, K.; Podryabinkin, E.V.; Shapeev, A.V. The MLIP package: Moment Tensor Potentials with MPI and Active Learning. *Mach. Learn. Sci. Technol.* **2021**, *2*, 025002.

28. Podryabinkin, E.V.; Shapeev, A.V. Active learning of linearly parametrized interatomic potentials. *Comput. Mater. Sci.* **2017**, *140*, 171–180. [CrossRef]

29. Mortazavi, B.; Novikov, I.S.; Podryabinkin, E.V.; Roche, S.; Rabczuk, T.; Shapeev, A.V.; Zhuang, X. Exploring phononic properties of two-dimensional materials using machine learning interatomic potentials. *Appl. Mater. Today* **2020**, *20*, 100685. [CrossRef]

30. Plimpton, S. Fast Parallel Algorithms for Short-Range Molecular Dynamics. *J. Comput. Phys.* **1995**, *117*, 1–19. [CrossRef]

31. Mortazavi, B.; Silani, M.; Podryabinkin, E.V.; Rabczuk, T.; Zhuang, X.; Shapeev, A. V First-Principles Multiscale Modeling of Mechanical Properties in Graphene/Borophene Heterostructures Empowered by Machine-Learning Interatomic Potentials. *Adv. Mater.* **2021**, *33*, 2102807. [CrossRef] [PubMed]

32. Mortazavi, B.; Shahrokhi, M.; Shojaei, F.; Rabczuk, T.; Zhuang, X.; Shapeev, A.V. A first-principles and machine-learning investigation on the electronic, photocatalytic, mechanical and heat conduction properties of nanoporous C5N monolayers. *Nanoscale* **2022**, *14*, 4324–4333. [CrossRef] [PubMed]

33. Silvi, B.; Savin, A. Classification of Chemical-Bonds Based on Topological Analysis of Electron Localization Functions. *Nature* **1994**, *371*, 683–686. [CrossRef]

34. Yue, Q.; Chang, S.; Kang, J.; Qin, S.; Li, J. Mechanical and Electronic Properties of Graphyne and Its Family under Elastic Strain: Theoretical Predictions. *J. Phys. Chem. C* **2013**, *117*, 14804–14811. [CrossRef]

35. Rawat, A.; Jena, N.; Dimple, D.; De Sarkar, A. A comprehensive study on carrier mobility and artificial photosynthetic properties in group VI B transition metal dichalcogenide monolayers. *J. Mater. Chem. A* **2018**, *6*, 8693–8704. [CrossRef]

36. Salavati, M.; Rabczuk, T. First-principles investigation of N-triphenylene-graphdiyne nanosheets as an anode material for Na, K, Mg and Ca storage. *Comput. Mater. Sci.* **2019**, *169*, 109093. [CrossRef]

37. Mortazavi, B.; Shahrokhi, M.; Madjet, M.E.; Makaremi, M.; Ahzi, S.; Rabczuk, T. N-, P-, As-triphenylene-graphdiyne: Strong and stable 2D semiconductors with outstanding capacities as anodes for Li-ion batteries. *Carbon* **2019**, *141*, 291–303. [CrossRef]

38. Li, C.; Zhang, X.; Wang, K.; Sun, X.; Ma, Y. High-power and long-life lithium-ion capacitors constructed from N-doped hierarchical carbon nanolayer cathode and mesoporous graphene anode. *Carbon* **2018**, *140*, 237–248. [CrossRef]

39. Tang, Y.; Wang, X.; Chen, J.; Wang, X.; Wang, D.; Mao, Z. PVP-assisted synthesis of g–C3N4–derived N-doped graphene with tunable interplanar spacing as high-performance lithium/sodium ions battery anodes. *Carbon* **2021**, *174*, 98–109. [CrossRef]

40. Wang, Z.; Qie, L.; Yuan, L.; Zhang, W.; Hu, X.; Huang, Y. Functionalized N-doped interconnected carbon nanofibers as an anode material for sodium-ion storage with excellent performance. *Carbon* **2013**, *55*, 328–334. [CrossRef]